New insights of Auger spectroscopy for the identification of Fe-Si compounds in iron/glass corrosion systems at nanoscale

Charly Carrière, Florence Mercier, Muriel Bouttemy, Eddy Foy, Xavier Crozes, Arnaud Etcheberry, Delphine D. Neff, Isabelle Monnet, Philippe Dillmann

New insights of Auger spectroscopy for the identification of Fe-Si compounds in iron/glass corrosion systems at nanoscale

Charly CARRIERE[(1)], Florence MERCIER[(1)], Muriel BOUTTEMY[(2)], Eddy FOY[(1)], Xavier CROZES[(3)]
Arnaud ETCHEBERRY[(2)], Delphine NEFF[(1)], Isabelle MONNET[(4)], Philippe DILLMANN[(1)]

(1) LAPA-IRAMAT, NIMBE, CEA, CNRS, Université Paris-Saclay, CEA Saclay, 91191 Gif-sur-Yvette France
(2) Institut Lavoisier de Versailles (ILV), Université Paris-Saclay, CNRS-UVSQ, 45 av. des Etats-Unis, Versailles, 78035, France
(3) EDF Lab Les Renardières, Département Matériaux et Mécanique des Composant, Site des Renardières, 77818 Moret-Sur-Loing Cedex
(4) Centre de Recherche sur les Matériaux, les Ions et la Photonique (CIMAP), CEA-CNRS-ENSICAEN, BP 5133, Bd Henri Becquerel, F-14070 Caen cedex 5, France

ABSTRACT

In the context of high-level radioactive wastes (HLW) storage, long term alteration of glass and corrosion of metallic containers leads to the formation of sub-micrometric phyllosilicate phases in the iron Corrosion Product Layer (CPL). The nature of these phases, their properties (porosity, electronic, passivation…) and their spatial distribution must be identified to determine their exact role in the iron corrosion process and to efficiently predict the long-term alteration of nuclear wastes package. In this work, the capabilities of localized Auger spectroscopy, combining surface chemical determination and high spatial resolution, to characterize these phyllosilicate phases is presented. In the present context, the main challenge to overcome was the insulating character of the different compounds and samples, presenting a real disadvantage for Auger implementation. A specific experimental protocol had to be developed to enable acquiring exploitable spectra at sufficiently high resolution to obtain identifiable fingerprints. The main Si-KLL Auger transition of different types of phyllosilicates representative of those encountered in the CPL of the glass-iron systems was acquired to determine if different chemical signatures and chemical shifts could be observed in function of the structure of reference phyllosilicates phases. Indeed, the Si-KLL kinetic energy position value of the phyllosilicate increases with the structure according the following order: smectite group < chlorite group < serpentine group and different line shapes are observed. The significant contribution of the present study relies on the achievement of analyzing such insulating materials by Auger at nanometric scale using a new generation Auger nano-probe (spot size around 12 nm) without drastic preparation requirements, enabling to constitute a Si-KLL Auger data base of phyllosilicates. Thanks to this preliminary analytical approach, the Si-KLL fingerprint measured in the CPL of the glass/iron system altered in an anoxic reactor at 90°C in synthetic

Callovo-Oxfordian (COx) clay-based groundwater solution could be identified as serpentine phyllosilicate. Transmission electron microscopy (TEM) analysis was also used to characterize phyllosilicate and reinforce the AES approach identification, confirming the presence of serpentines.

KEY-WORDS

Scanning Auger electron Microscopy (SAM), nanometric scale, phyllosilicates, iron anoxic corrosion, nuclear waste storage, AES analysis of insulating surfaces, serpentine

1. INTRODUCTION

In France, the strategy to manage high level radioactive wastes (HLW) is the disposal in anoxic medium in deep geological formation. The containment concept is based on multi-barriers with different kind of materials, as vitrified wastes, metal containers (stainless steel, carbon steel) confined in a low permeability host rock (Callovo Oxfordian argillite) [1]. The primary concern is to guarantee a low level of environmental and human contamination by radionuclides at short, intermediate and geological timescales. The assessment of the long-term behavior of the nuclear waste and the disposal materials are required in order to demonstrate the safety of this strategy and to guarantee the future geological disposal.

Particularly, the water coming from the deep geological medium could lead to the corrosion of the steel components. Furthermore, glass matrix may alter in presence of water. Then, glass long term alteration in the context of high-level radioactive waste (HLW) storage is influenced by near-field materials and environmental context. The increase of glass alteration rate in presence of iron, which comes from steel overpack, could be attributed to the precipitation of iron silicate species. They precipitate in the presence of ferrous ions released by corrosion of iron metal and silicon ions induced by the glass dissolution. The formation of these neoformed phases modifies the chemical equilibria in the aqueous solution and could act as a "silicon pump" and increase the glass alteration.

In the studies of McVay and Buckwalter [2], the few previous leaching tests of nuclear glass in the presence of Fe have reported the precipitation of Fe-silicates, either crystallized or in the form of amorphous nanocolloids. Depending on the alteration conditions, as for example pH and temperature, the Fe-silicate neoformed phases in the glass/iron or clay/iron systems can have various structures [3,4,5,6,7,8,9,10]. The presence of such neoformed phases in the glass alteration layer and in the iron corrosion product layer (CPL) conditions the degradation of the embedding materials of the nuclear waste package. They influence the glass alteration kinetics and have a role in the iron corrosion by forming a passivating layer or a barrier layer, changing the electronic properties or porosity of the corrosion product layers... Fe-silicates are therefore to be taken into account when considering the long-term behavior of nuclear waste package in deep geological conditions. For this reason, a crucial question should be addressed: what is the nature of these Fe-silicates neoformed at the glass surface and in the CPL formed on the metal? The identification of these phyllosilicates has to be performed to determine the properties of the alteration layers and their role in the iron glass alteration processes.

In addition to the context of nuclear industry, the study of phyllosilicate phases in the iron corrosion product layers finds also applications in domains where iron or steel is in contact with silicon from soil (clays, silica,…) and can concern ferrous objects buried in deep anoxic media as it is the case of archaeological objects from the anoxic site of Glinet on which Si was evidenced in the CPL [11]. The study of phyllosilicates is also of interest for Earth and Planetary Science, because the identification of the nature of these phases in meteorites permits to understand processes such as fluid-mediated alteration

on their parent bodies. For example, Lee et al. [12] characterized two phyllosilicate-bearing Antarctic meteorites by Transmission Electron Microscopy (TEM) and showed that Mg-rich aggregates are composed of lath-shaped serpentine crystals with ~0.73 nm basal spacing which are typical of the products of low temperature aqueous alteration within asteroidal parent bodies.

Actually, the crystalline nature of Fe-silicates is difficult to identify because of their submicron size. Consequently, macroscopic methods as X-Ray powder diffraction are not efficient. Other microscopic structural methods as Raman spectroscopy are also very limited because of high fluorescence signal caused by the presence of fluorescing trace elements in these media, and also the relatively distorted nature of silicate phases. Iron silicates in glass/iron systems were evidenced at nanometer scale by Scanning Transmission X-ray Microscopy (STXM) at the Fe L- or Fe K- or Si K- edges [13,14,15,16,9,10] and Transmission Electron Microscopy (TEM) [5,6,16,17]. However, these techniques need complex sample preparation under FIB thin films. For all these reasons, a multi-technique approach is beneficial to bring complementary information, also at different scales, and identify possible artifacts of preparation or analysis itself. Few laboratory techniques are able to reach nanometric resolution and inform about the local nature of the silicate phases in such complex system. To that purpose, Auger electron spectroscopies offer a good compromise as the samples do not need especially to be prepared under FIB slides at first sight, and present suitable spatial resolution with ultimate resolution of 8 nm while bringing chemical information. However, a special care has to be taken for surface preparation, in particular concerning carbon contamination, the Auger electrons being only collected within the first 4-5 nm of the material.

Studies related to the investigation of phyllosilicates by electron spectroscopies are rather rare probably because of the charge-up under beam associated to these non-conductive materials. By X-ray Photoelectron Spectroscopy (XPS), some studies are reported [18,19] but the large spatial resolution of XPS would not permit to characterize phyllosilicates phases of submicron size in our glass/iron/clay system. Concerning AES, the studies related to the investigation of phyllosilicates are less common than by XPS probably because the incident electron beam favoring charge accumulation, even more pronounced with the new generation nano-probe, and an increase of the charge-up of the insulating materials. Although several approaches exist to analyze insulators with AES [20], the only reported studies on this type of surfaces are devoted to the determination of elementary ratios as Fe/Si and Mg/Si in submicron-sized presolar grains in chondrites in order to have an insight of their aqueous and thermal alteration history [21,22]. Other authors used AES to enable deductions about the chemical state of silicon, but it concerned Fe-Si standards oxidized in CO_2 or air at 500°C [23]. In the present paper, Auger Electron Spectroscopy (AES) implemented with a nano-probe was used to: (1) obtain spectral Si-KLL fingerprints of different phyllosilicates representative of the neoformed phases reported in the alteration of glass/iron systems and consequently constitute an Auger data basis, currently nonexistent, for the iron phyllosilicates; and (2) identify what are the phyllosilicates formed in the CPL of a “real” sample constituted of an iron/glass system altered in anoxic reactor at 90°C during thirty months studied

in the frame of the nuclear context. Finally TEM in High Resolution is used to identify phyllosilicates and corroborate the Auger results, attesting also that the initial information are preserved and not modified under beam irradiation.

2. MATERIALS AND METHODS

2.1. Materials

Two types of samples were analyzed:

(1) reference phases of phyllosilicates for the determination of their Auger spectral fingerprints and the constitution of a spectral database for this type of compounds;

(2) an experimental sample constituted of a glass/iron system altered in representative conditions of the future French nuclear waste disposal and for which was researched the nature of the iron silicate phases present in the corrosion product layer.

Reference phyllosilicates phases

Phyllosilicates are composed of a pile-up of tetrahedral (T) and octahedral (O) layers. They are classified according to the type of arrangement which characterizes their group (TO, TOT or TOT:O) and inside each group, some subgroups are evidenced in function of the nature of the octahedral layer (di octahedral or tri octahedral). Reference phyllosilicate phases were chosen according to those evidenced from the literature on glass/iron or clay/iron systems systems [5,6,9,10,13,14,15,16,17]. These phases are reported in the Table 1 with their silicate group, their formula and their origin. The three groups of phyllosilicate are represented: TO group with the serpentines (berthierine and greenalite), TOT group with smectites (nontronite Garfield and saponite B46), and TOT:O group with chlorite (chamosite and chlorite CCa2). Berthierine, greenalite and chamosite come from Excalibur Mineral Corporation. Garfield nontronite provides from Garfield, Washington (USA) and saponite B46 is an autohydrothermal ferroan saponite [24].

The insulating character of the phyllosilicates did not enable to directly perform Auger analyses. A specific preparation methodology, detailed later on, was developed to minimize the charge accumulation and permit analyses without charge compensation leading to Auger peaks enlargement.

Experimental sample

The experimental sample corresponds to a sandwich of four sections in contact of the materials tested (about 1 cm × 1 cm with a thickness of 1 mm): 309S stainless steel/SON68 glass/SON68 glass/carbon steel (figure 1). The inactive nuclear glass SON 68 is a borosilicate glass with stable fission products (such as Zr, Cs, Ce, Nd and other) [25]. The pile-up is put into a stainless steel cell containing Bure argillite and is altered under anoxic and carbonated medium in an anoxic reactor during 28.5 months at 90°C and 8 bars in a synthetic Callovo-Oxfordian (COx) clay-based groundwater solution. The solution

was prepared from the groundwater composition calculated at equilibrium with COx claystone at 50°C [26]. After the experiment, the sample was prepared as transverse sections and polished to 1 µm roughness to perform analysis mainly at iron/glass 2 interface.

2.2. Analytical techniques

Field Emission Scanning Electron Microscopy (FESEM)

Backscattered Electron (BSE) imaging and compositional analysis of the CPL by Energy Dispersive Spectrometry (EDS) were obtained on a Field Emission Scanning Electron Microscope (FESEM) JEOL JSM-7001F. Incident acceleration voltage of 15 kV and a beam current of 12 nA were chosen. A carbon-coating layer of 15 nm was applied on the sample surface before their analysis.

µRaman Spectroscopy (µRS)

µRS measurements were carried out via an Invia Reflex® spectrometer with an excitation wavelength of 532 nm. The laser power was filtered down to 0.1 mW and the spectra were recorded with a resolution of 2 cm^{-1}. The beam diameter as well as the probed depth were about 1 µm. The spectrometer calibration was obtained from a silicon wafer on the 520.5 cm^{-1} peak. Acquisition and treatment of the spectra were obtained with the software Wire 3.4®. The spectra are presented without smoothing or line fitting.

Auger Electron Spectroscopy (AES)

Phyllosilicates characterization is a challenging field of investigation for Auger Electron Spectroscopy, especially at local scale, as such compounds are insulating and require not only adapted experimental settings strategy but also a specific preparation to enable their analysis. Indeed the electron induced Auger process by nature is more favorable for metals and semi-conductors materials analysis [27,28]. Nevertheless, these considerations do not signify that Auger analyses on insulating sample cannot be achieved but are arguments explaining why Auger is not, at first sight, the predilection method for phyllosilicates chemical characterization. Mainly two possibilities are classically employed, one consisting to use of a charge compensation gun and the other one to increase the specimen tilt angle in order to get the condition of glancing incidence of the primary beam and facilitates the flow of accumulated loads on the surface [20].

In this work, to obtain signal on iron silicates, which are non-conductive, a thorough method was optimized for the Auger characterization of the surfaces. Firstly separate pellets were created with few milligrams of silicate. Diameter of each compact pellet measured 5 mm, and compaction load is about 2 tons, with a SPECAC® press. Then each pellet was embedded in conductive resin (PolyFast containing graphite powder) which polymerizes at 180°C. The characterization of the samples before and after embedding was carried out with XDR and µRaman to be sure that there is no modification of the phyllosilicate structure during the heating at this temperature. The attention was mainly focused on the

phyllosilicates from the serpentines and smectites groups that can be more sensitive to temperature compared to chlorites.

The six embedded phyllosilicate references were polished in ethanol to grade 4000 with SiC paper, and to 1 µm roughness with MD-nap disk. Gold coating (15 nm thick) was applied on samples to manage problems of charge accumulation. Then conventional Ar^+ ionic etching over 1 mm² was employed to reach the sample surface and Auger analyses were carried out in this zone close to the conductive resin to favor the electron discharge. Abrasion was stopped when the gold signal became practically undetectable but before total elimination of the C adventitious contamination, present at the sample surface before the gold encapsulation, to limit possible erosion artifacts and keep this element as reference for energy positioning. The reproducibility of the Auger analyses was then tested on the different phyllosilicates by comparing the Si-KLL spectra obtained from different zones.

For the experimental sample, all the final steps were the same except there was no preparation of the sample under pellet: gold was directly deposited on the polished transverse section.

Auger characterizations were performed at ILV (Versailles, France) with a JEOL JAMP 9500F nano-probe equipped with a patented "in-lens" Schottky field emission gun and a hemi-spherical analyzer (HAS). The ultimate resolutions specified of this equipment are 3 nm (25 kV, 10 pA) for SEM and 8 nm (25 kV, 1 nA) for AES. For the reference samples, not requiring particularly high spatial resolution, experiments were carried out at 15 kV, 4-9 nA, tilt 40° and defocused spots to limit charging effect and increase the signal-to-noise ratio. For the experiment sample, the same experimental parameters were used but operating with a focused electron beam leading to 12-15 nm spot size, the maximal analyzed depth being inferior to 4-5 nm. No charge compensation leading to peaks enlargement and energy shifts was used in experiments. Firstly a global spectrum named survey is obtained from 0 to 2100 eV with a step size of 1 eV, relative energy resolution dE/E of 0.5%, to identify the present elements and determine the composition (peak-to-peak intensity measurement on the derivative dN(E)/dE spectra corrected by the JEOL RSF sensitivity factors). This survey enables to ensure the nature of the phase by determining the Fe/Si and Fe/Al ratio and characteristic minor elements detection. The Si-KLL spectral windows are made between 1520 and 1640 eV to acquire the entire Si-KLL features with a 0.75 eV step size. The energy scale was calibrated with respect to the C-KLL carbon contamination position at 272 eV in the derivative dN(E)/dE mode to certify the energy value of the Si-KLL peaks. Both direct and derivative peaks are presented. The numerical differentiation is operated with a Savitzky-Golay method considering 9 points to preserve as much as possible the initial information. From the fine spectral variations visible on the direct and derivative Si-KLL peaks, easily evidencing peak shape changing relative to the chemical environment of silicon. Those spectroscopic signatures obtained on identified reference phyllosilicate compounds are then employed to identify whether a mixed phase is present or isolated ones.

TEM

Ultra thin section of 1 µm ± 0.2 µm was cut using a focused ion beam (FIB) on the region of interest to perform TEM analysis. The electron-ionic double column microscope is a FEI Helios Nanolab 660 from CIMAP/GANIL (Caen, France) with a variable acceleration voltage from 0.5 kV to 30 kV and an ion current from 1 pA to 65 nA. Final steps of thinning were done at very low voltage and current in order to limit the amorphization of the thin foil.

Transmission electron microscopy (TEM) is carried out at 200 keV with a JEOL 2010 F electron microscope equipped with a field emission gun at CIMAP/GANIL (Caen, France). It is also equipped with a diode EDAX X-ray microanalysis, which allows chemical analysis in addition to imaging or electron diffraction to characterize nanoscale phases. To confirm characterization, High Resolution (HRTEM) is used on silicate identified by AES. Aim is to observe the atomic structure which also informs about the crystalline organization of the observed phases. Measuring distance of the sheet (tetrahedral, octahedral and interfoliation distance) leads to the identification of specific phyllosilicate group. These d-spacing (d_{001}) is measured with the ImageJ software.

3. RESULTS AND DISCUSSION

Reference phyllosilicates phases

Figure 2 displays Auger widescan spectra of each phyllosilicate reference. If one do not take into account carbon (whose presence is due to inherent surface contamination at ambient atmosphere), main detected elements are O, Si and Fe, except for chlorite which contains Mg in place of Fe. Different C contents are visible depending on the erosion time employed to remove the metallization layer. Saponite contains both Mg and Fe. In addition to these main elements, metallic cations, such as Al, Na, Ca and/or Mg are also visible. By comparing their presence to the expected ones (Table 1) for each different phyllosilicates, the representativeness of the Auger spectrum is validated, and so, the analysis positioning for further Si-KLL region acquisition. Atomic ratios obtained from derivative signals are given in Table 2. The Oc content corresponds to an estimation of the O quantity in the material after correction from the O involved in the superficial contamination layer usually evaluated by a C/2 proportion.

Figure 3 presents the high energy resolution Si-KLL spectral window (1520 to 1640 eV) in direct and derivative mode and Table 3 gives the position of the corresponding extrema. The obtained Si-KLL maxima (direct mode) and minima (derivative mode) energy position values for each phyllosilicate group and the associated structure are given in Table 4. The y=0 intercepts values for dN(E)/dE spectra are also presented in the table and agree with the N(E) maxima positions. Those values depend on the chemical environment of silicon, and can be classified according to the group of the phyllosilicate: [1615.9 – 1616.2 eV] for the TO group (berthierine and greenalite), [1613.5 – 1614.2 eV] for the TOT:O group (chlorite and chamosite) and [1610.1 – 1613.3 eV] for the TOT group (nontronite and saponite).

TOT group < TOT:O group < TO group.

These results are in good agreement with the one of Wagner *et al.* [29]. These authors report the Si-KLL energy values for Al-silicates with a variable substitution of Si by Al in tetrahedral site, evidencing an energy shift toward the lower energies when the Al quantity increases and a direct link between the energy position of the peak and the phyllosilicates group. They explained this shift by the variation of the negative charges on the silica network: the less negative charges in the network, the highest is the Si-KLL energy position. In our case, let us consider a pile-up of phyllosilicate sheets. Among the three structures of the phyllosilicates (TO, TOT:O or TOT), the TOT structure presents the highest number of silicate tetrahedra then the greatest number of Si by Al substitution. Consequently, our observation agrees with the demonstration of Wagner et al., the Si-KLL energy value measured being lower for TOT crystalline structure than for TO and TOT:O ones. The number of silicon tetrahedra is the same for TOT:O and TO structures and consequently it is not possible to explain the differences in the Si-KLL energy value for these two structures as for TOT relatively to TOT:O and TO groups. However, the serpentines from the TO group as berthierine and greenalite are little substituted in silicate tetrahedra: this could explain the higher Si-KLL energy value for the TO crystalline structures compared to the TOT:O ones.

Experimental sample

Iron corrosion interface

SEM images and the EDS distribution maps of the different elements are displayed on Figure 4 for the CPL formed on the metal part at the vicinity of the pristine glass. The average thickness of the CPL is about 10 µm. The CPL is constituted of different elements (Table 5): mainly O, Fe, but also S, Ca, Zn and Si. Ca and Si come from the glass alteration or/and from the synthetic COx solution in equilibrium with the Bure argillite (forthcoming publication). Ca does not seem to be correlated with Si and S and is rather located in the internal part of the CPL.

Differences were evidenced between the internal and external parts of the CPL. Concerning Si, its concentration is higher in the internal part (5.6 wt. %) than in the external part (2.5 wt. %). The Fe/Si ratio is 11.2 and 9.3 respectively in the external and internal part of the CPL. These values are higher than the ratio of the phyllosilicates (Table 2). This can be explained by the fact that in the analyzed zone, iron-silicates are mixed with iron corrosion products and consequently the Fe content is overestimated. µRaman analyses (Figure 5) revealed the presence of carbonates (peak at 1083 cm^{-1}) corresponding to siderite $FeCO_3$ or Fe-Ca siderite and of magnetite Fe_3O_4 (peak at 666 cm^{-1}), two phases typical of iron corrosion in carbonated anoxic environment [11,30,31,32,33].

In their experiments carried out in similar conditions (glass/iron/clay setup reacting at 90°C for 6-18 months), De Combarieu *et al.* [8] showed that iron corrosion led to the formation of a layer containing mostly magnetite, siderite and Fe-rich phyllosilicates. The data concerning the average thickness of the

CPL and the nature of the corrosion products are also in agreement with those reported in the studies of Burger *et al.* [9] on the glass/iron/clay stack corroded in anoxic conditions for two years at 50°C in geological repository conditions. These authors evidenced that *in situ* corrosion of iron leads to the precipitation of new phases homogeneously made of magnetite and forming a corrosion product layer of average thickness of 15 µm. The CPL thickness is also coherent with the iron corrosion rates measured in clay water in close conditions [34,35].

Note that these analyses were performed in the internal part of the CPL (white rectangle on Fig. 8 close to iron), which contains silicon, in an attempt to identify the iron-silicate phases. Although the presence of silicon in the CPL was observed by SEM-EDS, the nature of the Si-bearing phase could not be evidenced by µRaman probably because these phases have an extremely weak Raman scattering or because of their submicron size and/or poorly crystallinity.

Iron-silicate investigation

To determine the chemical environment of Si, the internal part of the iron CPL containing the Si highest content was analyzed by scanning Auger electron microscopy (SAM) (Figure 6). SAM elemental maps of O, Fe and Si in this zone are displayed. The distribution of Si, although slightly intense, seems to be homogeneous in the CPL. The survey spectrum in this zone indicates the presence of Auger lines of O, Fe and C which is coherent with the presence of magnetite and carbonates observed by µRaman spectroscopy. The Auger line Si-KLL is also visible in this internal part of the ICP. Lastly, minor elements as S, Al and Na are also detected on this spectrum.

The Si-KLL peak in derivative mode is compared to the one obtained on the phyllosilicate references (Figure 7) to determine the chemical environment of Si. As observed, the spectrum fingerprint of the sample is clearly different from the ones of nontronite and berthierine (Fig. 7-a), chlorite and saponite (Fig. 7-c), as well as and chamosite (figure 7-b). On the contrary the experimental spectrum fits relatively well with the greenalite reference (figure 11-d) on both peak shape and maximum energy position criteria. The minimum position of the Si-KLL peak is located at 1613.7 eV and the maxima of the direct spectrum at 1603.3 eV. According to the positions obtained previously for the different groups of the reference phyllosilicates, this value corresponds to the TOT:O group and not of TO as expected for greenalite. However, the presence of Al can indicate a partial substitution of Si by Al in the tetrahedral layer of this phyllosilicate and consequently a small negative shift of the Si-KLL peak energy position energy compared to the value expected for the phyllosilicates of the TO group.

To confirm the presence of serpentine in the CPL, HRTEM is used after cutting a FIB foil precisely in the area where greenalite was identified by AES. TEM-EDX spectrum (Fig. 8-a) highlights the presence of O, Fe, Si predominantly, as well as some metal cations (Al, S, Zn). The presence of Cu is only due to the presence of the copper support grid of the FIB foil. HRTEM (Fig. 8-b) reveals characteristic sheets of clays, with reticular distances of 7 Å between the sheets, corresponding to d_{001} distance. This value is

characteristic of serpentine-kaolinites group [7,36,37,38]. Therefore the method of silicates identification at nanoscale by AES is validated by TEM analyzes, a technique more commonly used.

Serpentines have already been detected in iron/clay experiments. Indeed, Mosser-Ruck *et al.* [7] conducted experiments where Wyoming bentonite, which contains more than 85 wt% of smectites, was in contact with iron (metal and magnetite) at different temperatures (80°C, 150°C and 300°C) in a carbonated medium at neutral pH. After several months at 80°C and 150°C, the silicate phases detected were trioctahedral serpentines (berthierine, cronstedtite) for Fe/C ratios> 0.5. According to these authors, temperature is one of the most important parameters controlling the smectite transformation of argillite to form serpentines. These results are coherent with the one presented by Perronet *et al.* [39], who carried out similar experiments at 80°C. For Fe/clay ratios ranging from 1/7.5 to 1/3, the smectites were altered and the product obtained corresponded to serpentines (berthierine presumably). At the Fe/clay ratio = 1/3, 50% of the smectites were consumed to form serpentines with a mixture of Fe(II) and Fe(III) in the octahedral sites.

Pignatelli *et al*. [4,5] proposed experiments in which the COx argillite was in contact with metallic iron (Fe/argilite ratio = 0.5) for several months at neutral pH under anoxic conditions. The objective was to verify the impact of temperature on the destabilization of COx argillite associated with the formation of new silicate phases. For this purpose the authors started the tests at 90°C and cooled them gradually, with a step of 10°C to reach 40°C. At each temperature drop of 10°C, the experimental device was analyzed. The results indicated that at 90°C quartz and smectites were destabilized and that the product obtained corresponded to iron-rich serpentine. It was from 80°C to 60°C that cronstedtite was best crystallized, with greenalite formation occurring at 70°C. The stability limit of the serpentines was fixed at 50°C since they are almost no longer detected at 50°C and 40°C.

The studies cited above have shown that iron serpentines are preferentially formed at 90°C, and at this temperature they are stable over time. Other authors [6,13,40] seem to confirm their presence during iron/clay alteration. The study presented in this paper formally shows that nanocrystalline Fe-rich serpentines (greenalite) crystallized in iron corrosion products during glass/iron/clay alteration.

4. CONCLUSION AND FURTHER WORK

By means of a thorough but relatively easy experimental protocol, making possible the analysis of insulating phyllosilicate phases by Auger spectroscopy, AES is a powerful technique to determine the Si-KLL Auger fingerprint of various phyllosilicates and consequently the nature of these phases at a submicron scale.

A spectra database of the Si-KLL Auger transitions of different types of phyllosilicates representative of those encountered in the CPL of the glass-iron systems is constituted. Identifiable fingerprints are

obtained with specific lineshapes and kinetic energy positions depending on the environment around Si atoms.

Then, the Si-KLL energy value can be related to the structure of the phyllosilicate and it varies according the following order: TOT group < TOT:O group < TO group. This study brings a first data base on the Auger Si-KLL energy values of the phyllosilicates.

A practical case of corrosion was considered through the study of the glass/iron system altered during thirty months at 90°C in synthetic Callovo-Oxfordian (COx) clay-based groundwater solution under anoxic environment. Silicon is present in the iron CPL and can come from glass alteration or/and from solution. Fe-Si-O neoformed phases corresponding to serpentines group could be identified in the iron CPL with the two nanometric techniques AES and TEM.

Further studies will be carried out to extend the AES database for phyllosilicates. The continuation of this study will be focused on some crucial points for a better understanding of the behavior of glass/iron systems in nuclear context: determination of the origin of Si in the neoformed phyllosilicates (water solution in equilibrium with clay and/or glass hydrolysis), influence of temperature and of the nature of the corrosion products (magnetite, siderite) on formed phyllosilicates.

Acknowledgment

We thank Emmanuel Gardes and Delphine Levavasseur for cutting and thinning the FIB foils. Isabelle Monnet (Cimap, GANIL, ENSICAEN, France) acknowledge the French state managed by the National Research Agency through the “Investissements d'Avenir” programme which reference is “ANR-11-EQPX-0020”, by the Normandie Region and the "Fonds Européen de Développement Régional" FEDER.

We also thank CNRS, CEA and Andra for the financial support of this work and EDF for providing us the glass/iron system.

References

[1] ANDRA Phenomenological Evolution of a Geological Repository, ANDRA. France (2005).

[2] G.L. McVay, C.Q. Buckwalter, Effect of iron on waste-glass leaching, Journal of the American Ceramic Society, 66.3 (1983) 170-174

[3] O. Bildstein, L. Trotignon, C. Pozo, M. Jullien, Modelling glass alteration in an altered argillaceous environment, Journal of Nuclear Materials 362 (2007) 493-501

[4] I. Pignatelli, E. Mugnaioli, J. Hybler, R. Mosser-Ruck, M. Cathelineau, N. Michau, A multi-technique characterization of cronstedtite synthetized by iron-clay interaction in a step-by-step cooling procedure, Clays and Clay Minerals 61.4 (2013) 277-289

[5] I.Pignatelli, F. Bourdelle, D. Bartier, R. Mosser-Ruck, L. Truche, E. Mugnaioli, N. Michau, Iron-clay interactions: detailed study of the mineralogical transformation of claystone with emphasis on the formation of iron-rich T-O phyllosilicates in a step-by-step cooling experiment from 90°C to 40°C, Chemical Geology 387 (2014) 1-11

[6] C. Rivard, M. Pelletier, N. Michau, A. Razafitianamaharavo, I. Bihannic, M. Abdelmoula, J. Ghanbaja, F. Villieras, Berthierine-like mineral formation and stability during the interaction of kaolinite with metallic iron at 90°C under anoxic and oxic conditions, American Mineralogist 98 (2013) 163-180

[7] R. Mosser-Ruck, M. Cathelineau, D. Guillaume, D. Charpentier, D. Rousset, O. Barres, N. Michau, Effects of temperature, pH, and iron/clay and liquid/clay ratios on experimental conversion of dioctahedral smectite to berthierine, chlorite, vermiculite or saponite, Clays and Clay Minerals 58.2 (2010) 280-291

[8] E. Burger, D. Rebiscoul, F. Bruguier, M. Jublot, J. E. Lartigue, S. Gin, Impact of iron on nuclear glass alteration in geological repository conditions: a multiscale approach, Applied Geochemistry 31 (2013) 159-170

[9] P. Dillmann, S. Gin, D. Neff, L. Gentaz, D. Rebiscoul, Effect of natural and synthetic iron corrosion products on silicate glass alteration, Geochimica et Cosmochimica Acta 172 (2016) 287-305

[10] C. Carriere, D. Neff, E. Foy, C. Martin, Y. Linnard, N. Michau, J. Dynes, P. Dillmann, Influence of iron corrosion on nuclear glass alteration processes: nanoscale investigations of the iron-bearing phases, Corrosion Engineering Science and Technology 52 (2017) 166-172

[11] M. Saheb, D. Neff, P. Dillmann, H. Matthiesen, E. Foy and L. Bellot-Gurlet, Multisecular corrosion behaviour of low carbon steel in anoxic soils: Characterisation of corrosion system on archaeological artefacts, Materials and Corrosion 60.2 (2009) 99-105

[12] M. R. Lee, P. A. Bland, G. Graham, Preparation of TEM samples by focused ion beam (FIB) techniques: applications to the study of clays and phyllosilicates in meteorites, Mineralogical Magazine 67.3 (2003) 581-592

[13] M.L. Schlegel, C. Bataillon, K. Benhamida, C. Blanc, D. Menut, J.-L. Lacour, Metal corrosion and argillite transformation at the water-saturated. Appl. Geochem., 23 (2008) 2619– 2633

[14] G. De Combarieu, M. L. Schlegel, D. Neff, E. Foy, D. Vantelon, P. Barboux, S. Gin, Glass-iron-clay interactions in a radioactive waste geological disposal: an integrated laboratory-scale experiment, Applied Geochemistry 26 (2011) 65-79

[15] A. Michelin, E. Burger, D. Rebiscoul, D. Neff, F. Bruguier, E. Drouet, P. Dillmann, S. Gin, Silicate glass alteration enhanced by iron: origin and long-term implications, Environmental science and Technology 47 (2013) 750-756

[16] A. Michelin, E. Leroy, D. Neff, J. J. Dynes, P. Dillmann, S. Gin, Archaeological slag from Glinet: an example of silicate glass altered in an anoxic iron-rich environment, Chemical Geology 413 (2015) 28-43

[17] M. Debure, L. De Windt, P. Frugier, S. Gin, P. Vieillard, Mineralogy and thermodynamic properties of magnesium phyllosilicates formed during the alteration of a simplified nuclear glass, Journal of Nuclear materials 475 (2016) 255-265

[18] R. Casanova, J. Mendialdua, A. Loaiza-Gil, A. Rodriguez, F. Rueda, Characterization of iron phyllosilicate catalysts by means of KLL Auger spectra of oxygen, Revista Latinoamericana de Metalurgia y Materiales, 22.2 (2002) 78-81

[19] C. Elmi, S. Guggenheim, R. Giere, Surface crystal chemistry of phyllosilicates using X-ray photoelectron spectroscopy: a review, Clays and Clay Minerals 64.5 (2016) 537-551

[20] D.R. Baer, A.S. Lea, J.D. Geller, J.S. Hammond, L. Kover, C.J. Powell, M.P. Seah, M. Suzuki, J.F. Watts, J. Wolstenholme, Approaches to analyzing insulators with Auger electron spectroscopy: Update and overview, Journal of Electron and Related Phenomena 176 (2010) 80-94

[21] C. Vollmer, P. Hoppe, F. J. Stadermann, C. Floss, F. E. Brenker, NanoSIMS analysis and Auger electron spectroscopy of silicate and oxide stardust from the carbonaceous chondrite Acfer 094, Geochimica et Cosmochimica Acta 73 (2009) 7127-7149

[22] C. Floss, P. Haenecour, Presolar silicate grains: Abundances, isotopic and elemental compositions, and the effects of secondary processing, Geochemical Journal 50 (2016) 3-25

[23] R.H. West and J.E. Castle, The Correlation of the Auger Parameter with Refractive Index: An XPS Study of Silicates Using Zr Lα Radiation, Surface and Interface Analysis 4.2 (1982) 68-75

[24] H.G. Dill, R. Dohrmann, S. Kaufhold, Disseminated and faultbound autohydrothermal ferroan saponite in Late Paleozoic andesites of the Saar-Nahe Basin, SW Germany: Implications for the economic geology of intermediate (sub)volcanic rocks, Applied Clay Science 51 (2011) 226-240

[25] T. Advocat, P. Jollivet, J. Crovisier, M. Del Nero, Long-term mechanisms in water for SON68 radioactive borosilicate glass. Journal of Nuclear Materials, 298.1 (2001) 55-62

[26] E. C. Gaucher, C. Tournassat, F. J. Pearson, P. Blanc, C. Crouzet, C. Lerouge, S. Altmann, A robust model for porewater chemistry of clayrock, Geochimica et Cosmochimica Acta 73 (2009) 6470-6487

[27] M. Prutton and M. M. El Gomati, Scanning Auger, Electron Microscopy, ED. John Wiley & Sons (2006)

[28] K. Tsutsumi, N. Ikeo, A. Tanaka and T. Tazawa, JEOL News 45.1 (2010) 47

[29] C. D. Wagner, D. E. Passoja, H. F. Hillery, T. G. Kinisky, H. A. Six, W. T. Jansen, J. A. Taylor, Auger and photoelectron line energy relationships in aluminum-oxygen and silicon-oxygen compounds, Journal of Vacuum Science and Technology 21.4 (1982) 933-944

[30] D. Neff, L. Bellot-Gurlet, P. Dillmann, S. Reguer, L. Legrand, Raman imaging of ancient rust scales on archeological iron artefacts for long-term atmospheric corrosion mechanisms study, Journal of Raman Spectroscopy 37 (2006) 1228-1237

[31] M. Hanesch, Raman spectroscopy of iron oxides and (oxy)hydroxides at low laser power and possible applications in environmental magnetic studies, Geophysical Journal International, 177.3 (2009) 941–948

[32] M. Saheb, D. Neff, L. Bellot-Gurlet and P. Dillmann, Raman study of a deuterated iron hydroxycarbonate to assess long-term corrosion mechanisms in anoxic soils, J. Raman Spectrosc. 42 (2011) 1100-1108

[33] Y. Leon, P. Dillmann, D. Neff, M.L. Schlegel, E. Foy, J.J. Dynes, Interfacial layers at a nanometre scale on iron corroded in carbonated anoxic environments. RSC Adv., 7.33 (2017) 20101–20115

[34] F. Papillon. M. Jullien. C. Bataillon. Carbon steel in compacted clay: two long term tests for corrosion prediction. In: Prediction of Long Term Corrosion Behavior in Nuclear Wastes System. Cadarache. France. EFC Series. vol. 36 (2003) 439–454

[35] N. Taniguchi. M. Kawasaki. S. Kawakami. M. Kubota. Corrosion behavior of carbon steel in contact with bentonite under anaerobic condition. Prediction of long term corrosion behaviour in nuclear waste systems*,* In: Proc. 2nd Int. Workshop on European Federation of Corrosion and ANDRA (2004)

[36] H.G. Changela, J.C. Bridges, Alteration assemblages in the nakhlites: Variation with depth on Mars. Meteoritics & Planetary Science, 45.12 (2010) 1847–1867

[37] L.J. Hicks, J.C. Bridges, & S.J. Gurman, Ferric saponite and serpentine in the nakhlite martian meteorites. Geochimica et Cosmochimica Acta, 136 (2014) 194–210

[38] F.J. Huertas, S. Fiore, J. Linares, In situ transformation of amorphous gels into spherical aggregates of kaolinite: A HRTEM study, Clay Minerals, 39.4 (2004) 423–431

[39] M. Perronnet, M. Jullien, F. Villiéras, J. Raynal, D. Bonnin, G. Bruno, Evidence of a critical content in Fe (0) on FoCa7 bentonite reactivity at 80 C, Applied Clay Science, 38.3 (2008) 187–202

[40] M.L. Schlegel, C. Bataillon, F. Brucker, C. Blanc, D. Prêt, E. Foy, M. Chorro, Corrosion of metal iron in contact with anoxic clay at 90 C: characterization of the corrosion products after two years of interaction, Applied Geochemistry, 51 (2014) 1–14

Captions for the illustrations

Figure 1: Schematic diagram of the experimental sample for the alteration experiment

Figure 2: Widescan spectra obtained for each phyllosilicate reference phase (dE/E of 0.5%)

Figure 3: High energy resolution Si-KLL direct and derivative spectra obtained on each phyllosilicate (dE/E = 0.35%). Spectra are shifted in ordinate direction for clarity reasons

Figure 4: SEM image in secondary electron and EDS distributions of the different elements constituting the iron CPL of the sample. White rectangles on the SEM image indicate the areas corresponding to the quantitative analysis

Figure 5: µRaman spectrum corresponding to the analysis of the iron CPL

Figure 6: SEM secondary electron images (a), AES maps of O, Fe and Si (b) in the internal CPL, survey spectrum and atomic composition corresponding to the spot in the zone (marked by the cross sign) in the internal CPL (c)

Figure 7: Comparison of the Si-KLL derivative signals of the CPL region with the phyllosilicate references ones: nontronite and berthierine (a); greenalite and chamosite (b); chlorite and saponite (c) and the best fit obtained with the reference greenalite (d)

Figure 8: TEM-EDS (a) and HRTEM (b) obtained precisely on serpentine identified by AES

Table 1: Reference phyllosilicates studied (silicate group, formula and origin).

Layer	Group	Chemical formulas • *from webmineral • **from Data Handbook for Clay Minerals (Van Olpen and Fripirat, 1979)	Provenance
TO	Berthierine Excalibur Trioctahedral Serpentine	$(Fe^{2+},Fe^{3+},Al,Mg)_{2-3}(Si,Al)_2O_5(OH)_4$*	Excalibur Mont St. Hilaire, Quebec, Canada
	Greenalite Trioctahedral Serpentine	$(Fe^{2+};Fe^{3+})_{2-3}Si_2O_5(OH)_4$*	Excalibur La Union, Murcia, Spain
TOT	Nontronite Garfield Dioctahedral Smectite	$Na_{0,3}Fe^{3+}{}_2(Si, Al)_4O_{10}(OH)_2.n(H_2O)$**	Garfield, Washington, USA
	Saponite B46 Trioctahedral Smectite l	$Ca_{0.3}(Fe^{2+},Mg,Fe^{3+})_3(Si,Al)_4O_{10}(OH)_2•4(H_2O)$*	Late Variscan Saar-Nahe Basin, SW Germany
TOT : O	Chamosite, Tri-trioctahedral Chlorite	$(Fe^{2+};Mg;Fe^{3+})_5Al(Si_3Al)O_{10}(OH;O)_8$*	Excalibur unspecified location. California or Wyoming, USA
	Chlorite CCa-2, Trioctahedral Chlorite	$Ca_{0.05}(Mg_{4.44}Al_{0.6}Fe_{3.47}{}^{3+}Fe_{3.02}{}^{2+}Ti_{0.06})(Si_{4.51}Al_{13.49}]O_{20}(OH)_{16}$ **	Flagstaff Hill, El Dorado County, California, USA

Table 2: Atomic ratios calculated with elementary composition (from widescan spectra after derivation of the signal) for each phyllosilicate. d. and n.d. for detected and non-detected, respectively

	C/O	Oc/Si	Fe/Si	Al/Si	Mg	Na	N	Ca
chamosite	1.1	3.1	1.5	1.1	d.	n.d.	d.	n.d.
nontronite	0.9	2.1	0.9	0.2	n.d.	d.	d.	n.d.
berthierine	0.2	5.3	1.2	0.5	d.	n.d.	d.	n.d.
greenalite	0.6	2.8	1.2	Al n.d.	d.	n.d.	n.d.	n.d.
chlorite	0.3	7.9	0.1	1.0	d.	n.d.	n.d.	n.d.
saponite	0.7	3.2	0.2	0.1	d.	n.d.	n.d.	d.

Table 3: Kinetic energy position of the Si-KLL maxima, minima and abscissa intercept measured on the derivative signal spectra obtained on Fig. 3

	Maxima position on the direct spectra (eV ± 0.2)	Minima position on the derivative spectra (eV ± 0.2)	I Intercept with the Y=0 axis on the derivative spectra (eV ± 0.2)
Nontronite	1603.8	1613.3	1604.0
Chamosite	1606.75	1613.5	1607.0
Chlorite	1603.3	1614.2	1602.9
Saponite	1604.3	1610.1	1604.1
Berthierine	1604.5	1616.2	1604.9
Greenalite	1605.35	1615.9	1605.3

Table 4: Si-KLL kinetic energy position values obtained for each phyllosilicate group and the associated structure

Phyllosilicate group	Si-KLL energy (eV)
TO	1615.9 – 1616.2 greenalite - berthierine
TOT :O	1613.5 – 1614.2 chamosite - chlorite
TOT	1610.1 – 1613.3 saponite - nontronite

Table 5: Composition (in wt.%) obtained from EDS in the internal and external CPL (white rectangles on Fig. 4)

CPL	O	Fe	Si	Al	Ca	Zn	S	Σ
external	42	28	2.5	0.7	21	3	1.5	98.7
internal	30	52	5.6	0.7	1.2	7.5	2	99

Illustrations

Figure 1:

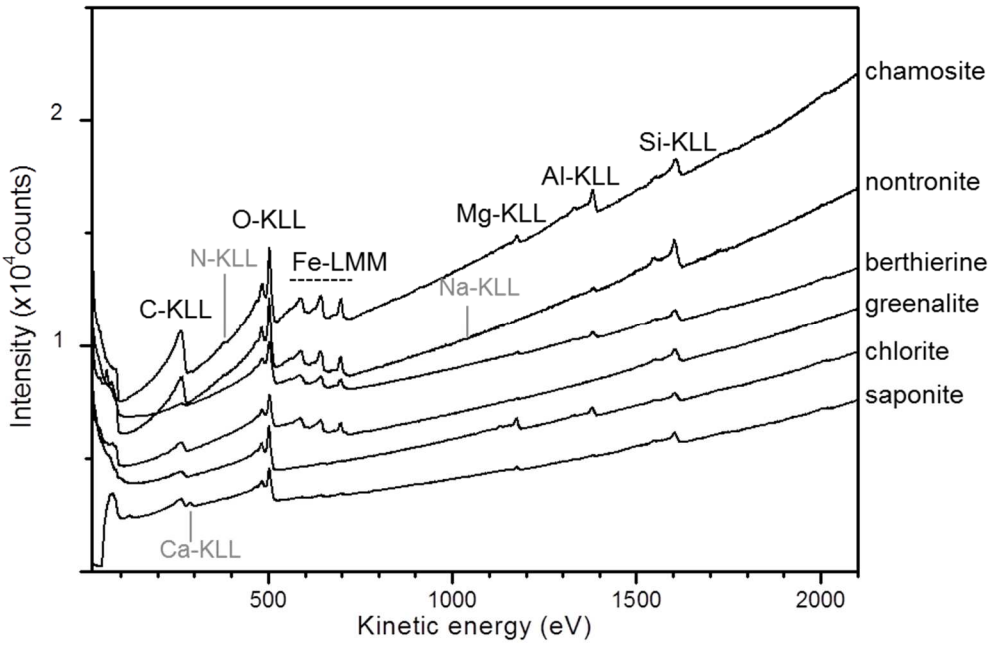

Figure 2:

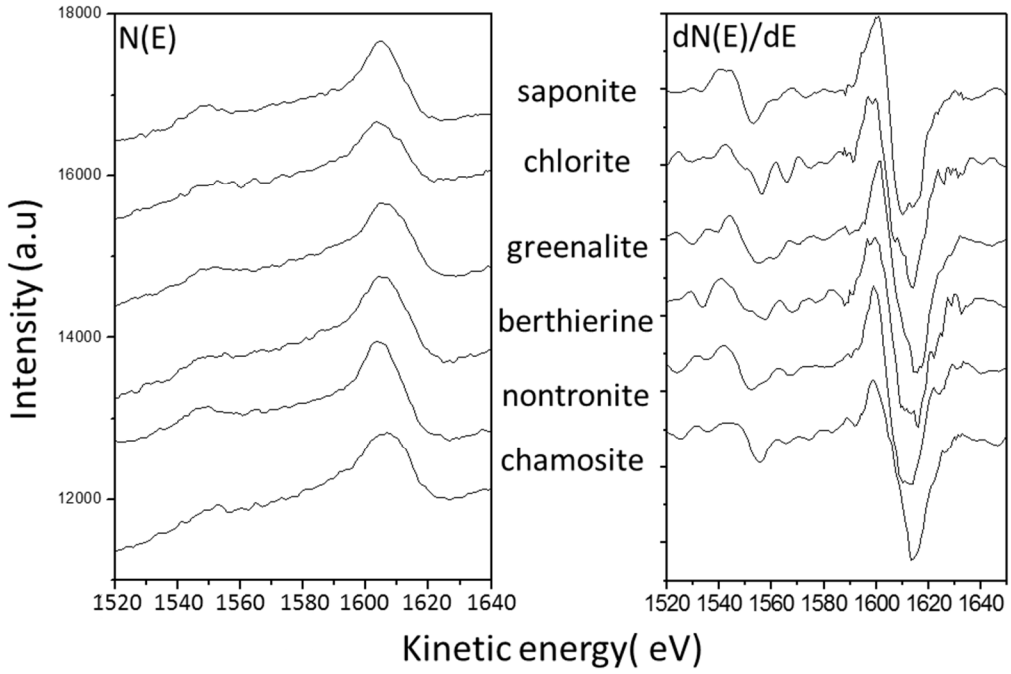

Figure 3:

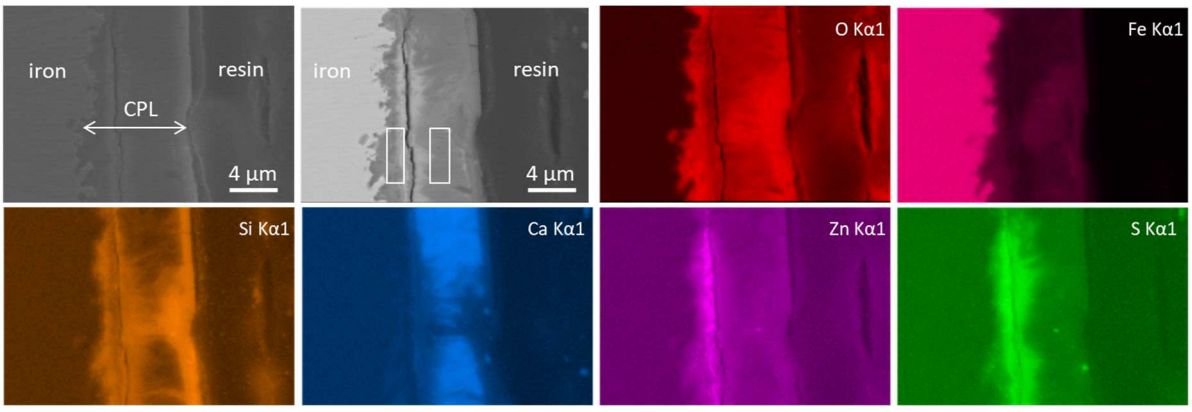

Figure 4:

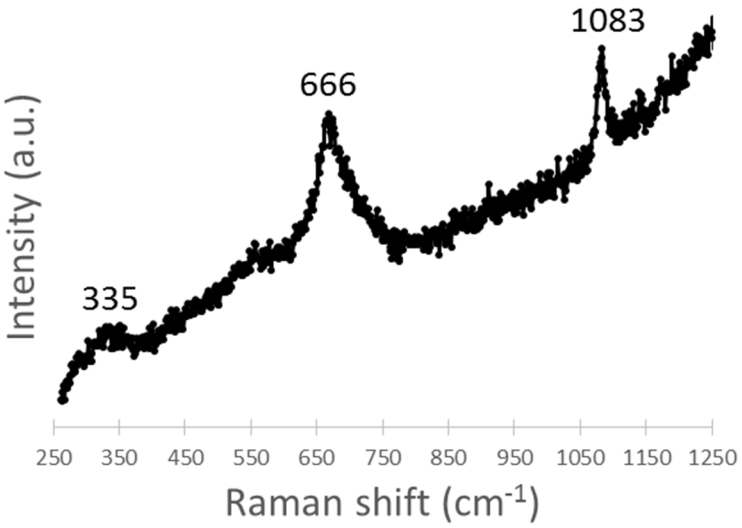

Figure 5:

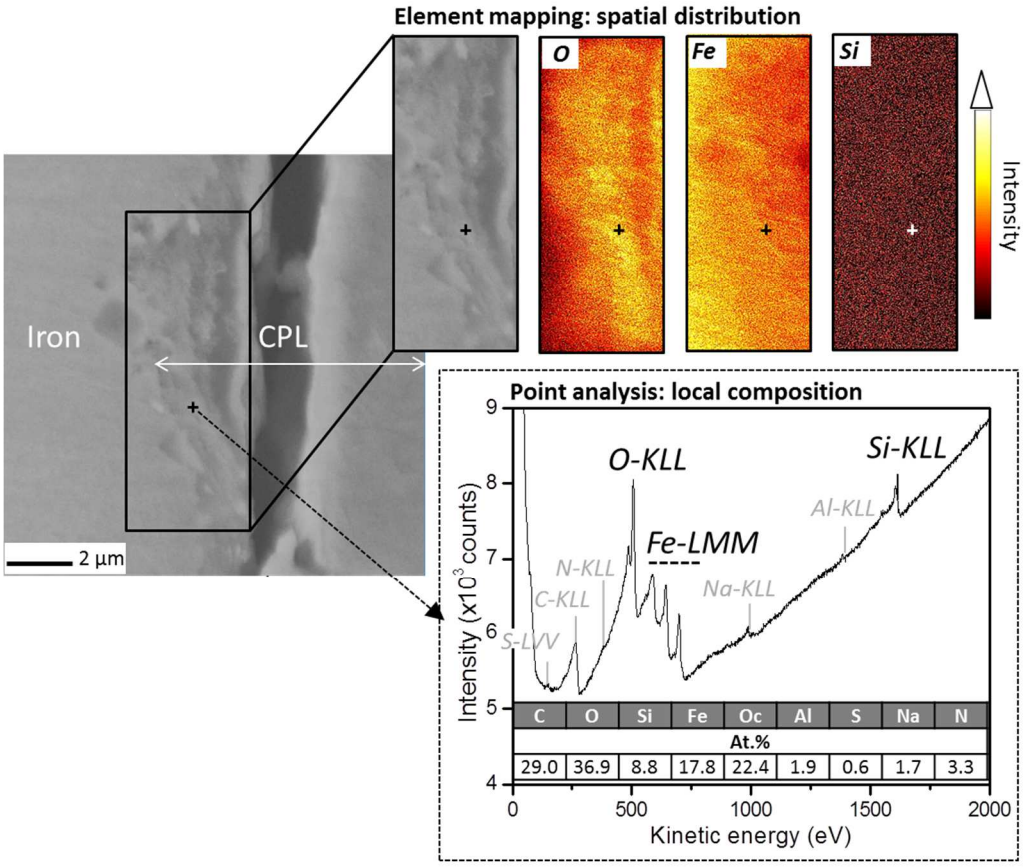

Figure 6:

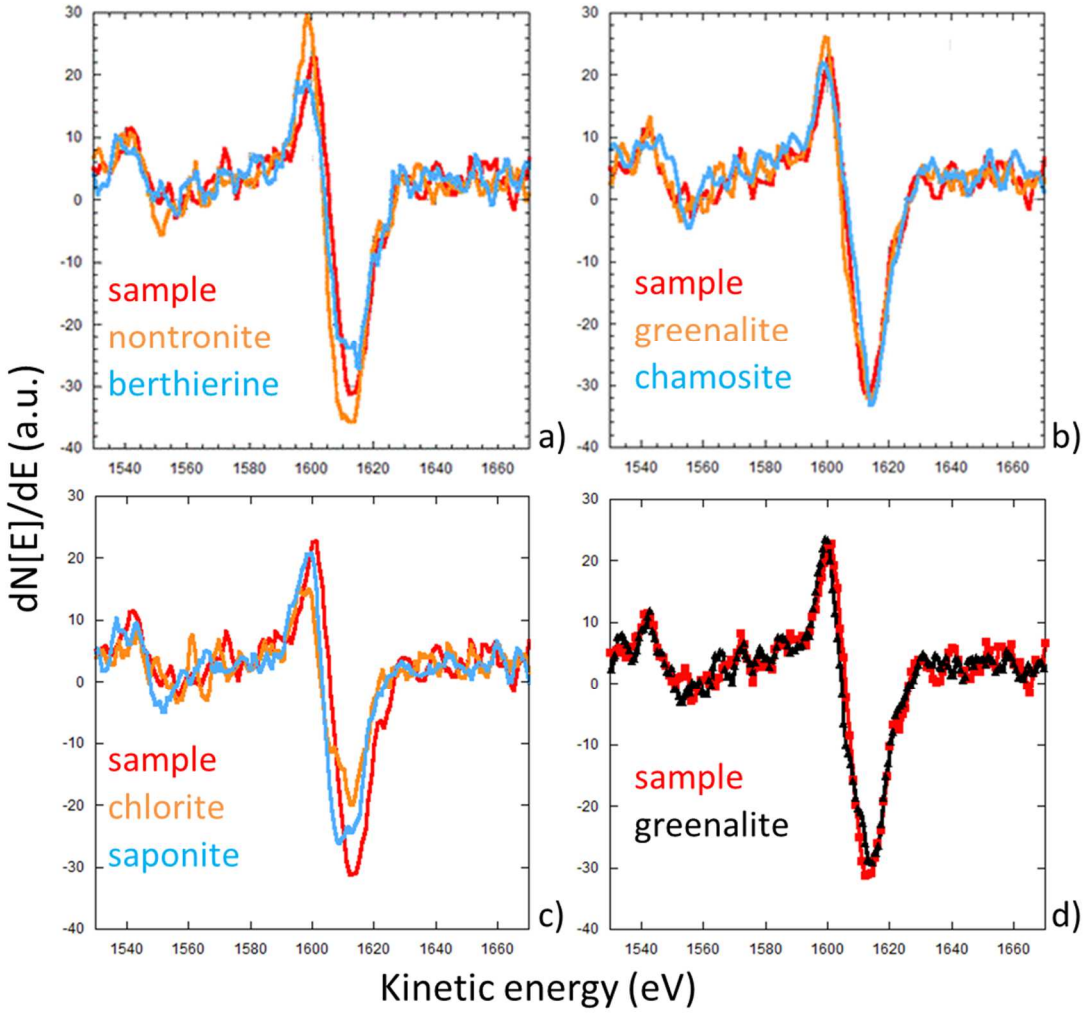
dN[E]/dE (a.u.)
Kinetic energy (eV)
sample
nontronite
berthierine
a)
sample
greenalite
chamosite
b)
sample
chlorite
saponite
c)
sample
greenalite
d)

Figure 7:

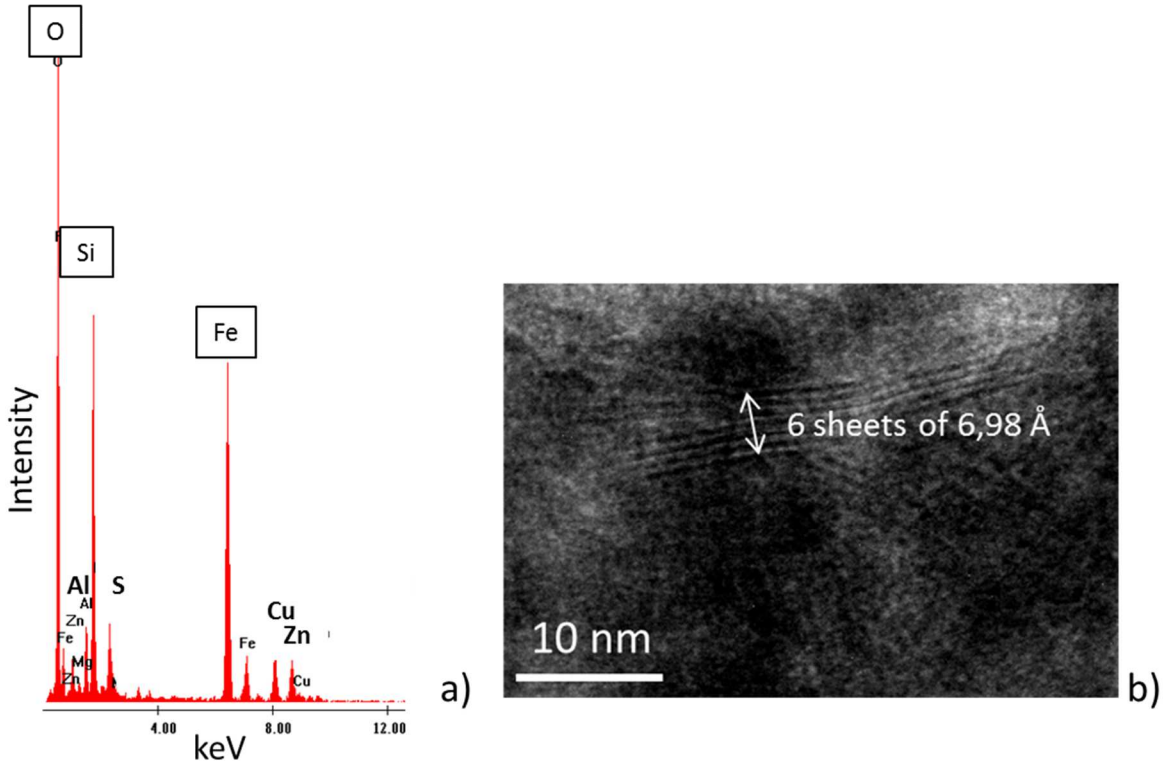
O
Si
Fe
Intensity
Al
S
Cu
Zn
Fe
Mg
Zn
4.00
8.00
12.00
keV
a)
6 sheets of 6,98 Å
10 nm
b)

Figure 8: